Catalysis Today 476 (2026) 115893

Contents lists available at ScienceDirect

Catalysis Today

journal homepage: www.elsevier.com/locate/cattod

Synthesis of Y-doped $ZnBi_2O_4$ spinel oxide and its application for the photocatalytic degradation of aqueous levofloxacin under sunlight

Maryam Rao [a], Muhammad Naeem [b], Adnan Ashraf [a,*], Muhammad Asam Raza [c], Wesam Abd El-Fattah [d], Mohammad Mahbubul Hassan [e,*]

[a] Department of Chemistry, The University of Lahore, Lahore, Pakistan
[b] School of Chemistry, University of the Punjab, Quaid-e-Azam Campus, Lahore 54590, Pakistan
[c] Department of Chemistry, University of Gujrat, Gujrat, Pakistan
[d] Department of Chemistry, College of Science, Imam Mohammad Ibn Saud Islamic University (IMSIU), P. O. Box 5701, Riyadh 11432, Saudi Arabia
[e] Fashion, Textiles, and Technology Institute, University of the Arts London, London E20 2AR, United Kingdom

ARTICLE INFO

Keywords:
Spinel oxide
Sunlight-driven photocatalysis
Levofloxacin
Photocatalytic degradation
Reusability of spent photocatalysts

ABSTRACT

The removal of antibiotic residues from drinking water is critical for public health to prevent long-term toxicological effects on humans and aquatic ecosystems. Spinel oxides are widely recognized as effective photocatalysts for their removal from water by photodegradation. In this work, we synthesized 1, 3, and 5% yttrium-doped $ZnBi_2O_4$ spinel oxides for the removal of levofloxacin (LVF) from water. The photocatalytic degradation of LVF under sunlight reached a maximum of 98.5% compared to 70.6% exhibited by the undoped $ZnBi_2O_4$ in 120 min for the 3% Y-doped $ZnBi_2O_4$ (YZBO-3), along with high TOC reduction. The Y^{3+}-doping created defects in the $ZnBi_2O_4$ lattice, creating oxygen vacancies and decreasing the band gap. The enhanced photodegradation exhibited by YZBO-3 compared to the undoped $ZnBi_2O_4$ can be attributed to improved charge separation, dopant solubility effects, and an increase in visible light absorption as suggested by XRD, Raman, and optical analyses. The results of radical trapping experiments indicate that hydroxyl (•OH) and superoxide anion ($\bullet O_2^-$) radicals play a crucial role in the photodegradation of LVF. The reusability and stability of the photocatalyst were assessed for five cycles, and the reduction in photodegradation efficiency was quite small after five cycles of recycling and reuse.

1. Introduction

The contamination of potable water by pharmaceutical waste is a serious concern as it can have unprecedented detrimental effects on human health [1,2]. There is already a shortage of drinking water in various parts of the world, and pollution of water can further worsen the situation. Many toxic compounds, such as metal ions, dyes, pharmaceuticals, and especially antibiotics originating from urban and industrial wastewater, may end up in water sources, polluting freshwater ecosystems [3,4]. A huge range of antibiotics is used for the treatment of a variety of diseases, and a portion of those unmetabolized drugs ends up in the environment through urine and feces, posing serious risks to ecosystems [5]. Fluoroquinolone-based antibiotics, such as levofloxacin (LVF), are frequently detected in the aquatic environment [6]. Current antibiotic removal technologies may include adsorption [7], microalgae-mediated technologies [8], biological treatment [9], membrane separation [10], and advanced oxidation processes (AOPs) [11]. While the AOP-based processes are highly effective in degrading antibiotics, they have a high operational cost. The other methods often suffer from drawbacks, such as incomplete or no degradation, removal process is very slow, and poor removal. In contrast, photocatalytic degradation offers advantages such as high degradation efficiency, eco-friendliness, and the capability of complete mineralization [12,13]. Photocatalysts harness light to trigger or accelerate chemical reactions without being consumed in the process, and therefore, they can be recycled and reused many times.

The sunlight-activated photocatalysts have a narrow band gap to absorb a broader spectrum of solar radiation compared to the UV-activated photocatalysts, minimizing the cost and the safety of the treatment [14]. While polyoxometalate photocatalysts offer excellent redox flexibility and strong Brønsted acidity, they have extremely low surface areas, limiting access to active sites; high solubility in polar

* Corresponding authors.
E-mail addresses: adnan.ashraf@chem.uol.edu.pk (A. Ashraf), mahbubul.hassan@arts.ac.uk (M.M. Hassan).

https://doi.org/10.1016/j.cattod.2026.115893
Received 22 February 2026; Received in revised form 7 June 2026; Accepted 8 June 2026
Available online 9 June 2026

solvents makes their recycling difficult, and they also show hydrolytic instability in strongly alkaline conditions [15]. Recently, spinel-type metal oxides with the general formula AB_2O_4 have drawn attention due to their high stability, ease of synthesis, and efficient photocatalytic activity [16,17]. Within this class, $ZnBi_2O_4$ has emerged as a promising photocatalyst due to its chemical stability, high photocurrent density, and band gap, which typically ranges from 2.78 eV to 2.87 eV, making it highly effective at absorbing visible light. It has been applied in diverse photocatalytic processes, including CO_2 reduction, hydrogen production, and the removal of dyes and drugs from water [18,19]. However, it suffers from low efficiency, which can be greatly improved by the incorporation of rare-earth metal dopants, heterojunction design, and the introduction of atomic-level structural imperfections by increasing oxygen vacancies [20,21]. Recently published research shows that europium and samarium-doped $ZnBi_2O_4$ exhibited enhanced charge separation, wider-spectrum light absorption, and higher photocatalytic activity under solar irradiation for the photodegradation of levofloxacin and moxifloxacin, respectively [22,23]. Doping also creates oxygen vacancies, which act as active sites and increase reaction molecule adsorption in many instances [24]. Rare-earth elements, especially yttrium, have attracted attention because of their unusual electronic configurations and capability to provide locally localized f-orbital states that can assist in the trapping of charge carriers and extend the life of photogenerated electrons and holes [25]. For example, yttrium, with its large ionic radius, ability to induce lattice distortion, and strong electron trapping ability, has shown beneficial effects in several spinel ferrite catalysts, including $MnFe_2O_4$ [27] and $Mg_{0.6}Zn_{0.4}Y_xFe_{2-x}O_4$ [28]. Similarly, Y^{3+} doping into the $ZnBi_2O_4$ structure might cause lattice distortion as the ionic radius of Y^{3+} is larger than that of Zn^{2+} and Bi^{3+}, leading to the generation of oxygen vacancies and overcoming the efficiency limitations of pure $ZnBi_2O_4$ [26]. Moreover, Y^{3+}-doped $ZnBi_2O_4$ was not reported for the photodegradation of LVF under sunlight irradiation. In this study, we synthesized yttrium-doped zinc bismuth spinel oxide via a hydrothermal route with varying yttrium concentrations (such as 1%, 3, and 5 mol%). The influence of yttrium substitution for Bi^{3+} on structural, morphological, magnetic, and photocatalytic properties was systematically investigated, with particular focus on antibiotic degradation under sunlight.

2. Materials and methods

2.1. Materials

Bismuth nitrate pentahydrate [$Bi(NO_3)_3 \bullet 5H_2O$, 98% purity] from UniChem (China), zinc nitrate hexahydrate [$Zn(NO_3)_2 \bullet 6\ H_2O$, 98% purity], yttrium nitrate hexahydrate [$Y(NO_3)_3 \bullet 6\ H_2O$, 99.8% purity], Sodium hydroxide (NaOH, 97.0% purity), and nitric acid (HNO_3, 70% purity) were purchased from Sigma-Aldrich (USA). Levofloxacin hemihydrate was procured from T.N. Pharmaceuticals Pvt. Ltd. (Pakistan). All chemicals used in this work were as-received.

2.2. Synthesis of Y-doped $ZnBi_2O_4$ (YZBO)

Pure $ZnBi_2O_4$ (ZBO) and 1, 3, 5% yttrium (Y^{3+}) doped $ZnBi_2O_4$ (YZBO) were synthesized by the hydrothermal method. A required amount of $Bi(NO_3)_3 \bullet 5\ H_2O$ was dissolved in 25 mL deionized water to prepare a 5 mmol solution, and dropwise, 3 M nitric acid was added to it until complete dissolution of all the chemicals was achieved and a transparent solution was formed. A stoichiometric amount of zinc nitrate was added to 25 mL of water to prepare a 2.5 mmol solution. It was added to the bismuth nitrate solution, and the mixture was stirred for 1 h. After 60 min of stirring, for 1, 3, and 5% doping of Y, a stoichiometric amount of yttrium nitrate ($Zn_{1-x}Bi_{2-2x}Y_{3x}O_4$, x = 0.01, 0.03, and 0.05) solution was added to it, and stirring was continued for a further 30 min. The pH of the above solution was adjusted to 9–10 using 0.1 N NaOH solution to promote uniform nucleation during the hydrothermal process, and this mixture was then transferred to a 100-mL autoclave and heated at 180 ℃ for 14 h for hydrothermal treatment. After which, the autoclave was cooled down to room temperature, and the YZBO was recovered through filtration using Whatman filter paper. Y^{3+} is likely incorporated into the $ZnBi_2O_4$ lattice by substitution at Bi^{3+} sites. The difference in ionic radius introduces lattice distortion and promotes the formation of oxygen vacancies to maintain charge neutrality. The prepared catalyst was washed several times with distilled water and finally with ethanol, and the final product was dried at 90 ℃ in an oven for 5 h. The obtained product was crushed into fine powder by using a pestle and a mortar, and then these powders were calcined at 500 ℃ for 4 h at the rate of 5 ℃/min. The calcination temperature of 500 °C was selected based on preliminary optimization and literature reports on $ZnBi_2O_4$ synthesis. This temperature is sufficient to promote crystallization of the spinel phase and remove residual nitrate species while minimizing excessive particle growth and agglomeration. The schematic illustration of the hydrothermal synthesis of Y-doped $ZnBi_2O_4$ is presented in Fig. 1.

2.3. Characterizations

The X-ray diffractometer (XRD) patterns of ZBO and various YZBO photocatalysts were recorded using a Bruker Powder X-ray diffractometer (XRD, Model: AXS D8 Advance, Bruker Corporation, Germany) using Cu Kα (40 kV, 30 mA) as the radiation source and NaI as the detector (scanning speed was 0.012°/s, 2θ from 20 ° to 80 ° by 0.012°/s). The catalysts were also characterized by Fourier transform infrared (FTIR) spectrometry using a JASCO FTIR (Model: NRS- 4100, Jasco International Co., Ltd., Japan). The elemental analysis of the prepared catalyst was conducted by a Hitachi scanning electron microscope (SEM, Model S3000N, Hitachi Corporation, Japan) fitted with a Bruker EDX detector. The UV–vis spectra of the synthesized photocatalyst were recorded on a Shimadzu UV-Vis spectrometer (Model: UV 1860, Shimadzu Corporation, Japan) from wavelengths of 200–800 nm.

2.4. Photocatalytic degradation of LVF

The photocatalytic performance of pure and Y-doped $ZnBi_2O_4$ was studied by conducting photocatalytic degradation of LVF under sunlight on 12th May 2025 (11:00 AM) on a sunny day at Lahore, Pakistan (31.428°N latitude, 74.241°E longitude) with peak hot day temperature 38–42 °C. The intensity of solar irradiance was not directly measured using a pyranometer. According to the local meteorological department, the sunlight intensity at that time was 0.79–0.95 kW/m^2. The photocatalytic degradation of LVF by Y-doped $ZnBi_2O_4$ under sunlight is illustrated by a schematic diagram in Fig. 2. For the photodegradation study, 100 mL aqueous solution of LVF with an initial concentration of 5 ppm was taken in a round-bottom flask, and 0.3 g/L ZBO or YZBO was added to it under magnetic stirring. The suspension was kept under dark conditions for 15 min to obtain adsorption-desorption equilibrium and also to measure the removal of LVF by adsorption rather than by photocatalytic degradation. The concentration of LVF was measured, and this concentration was considered the concentration at zero time for photocatalytic degradation. The LVF solution was then exposed to sunlight, and a 3–4 mL aliquot was collected from the reaction mixture after specified intervals. The concentration of LVF in solution was measured immediately at 278 nm using UV-Visible spectroscopy. All experiments were conducted under identical environmental conditions to ensure consistency of results, and the reported values represent the average of three independent measurements with corresponding standard deviations.

The role of the free radicals in the process of photocatalytic degradation was also determined by conducting free radical scavenger tests. The scavengers assessed were isopropyl alcohol (IPA), *para*-benzoquinone (p-BQ), Silver nitrate ($AgNO_3$), and EDTA, which were used for the scavenging of hydroxyl (•OH), superoxide ($\bullet O_2^-$), electrons (e^-), and holes (h^+), respectively. The stability of the photocatalyst was

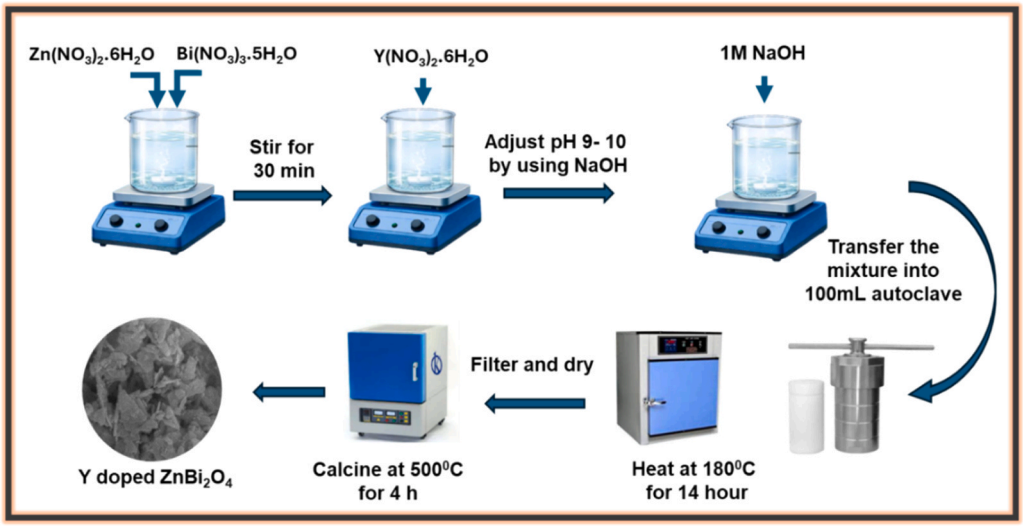

Fig. 1. Schematic illustration of hydrothermal synthesis of Y-doped $ZnBi_2O_4$.

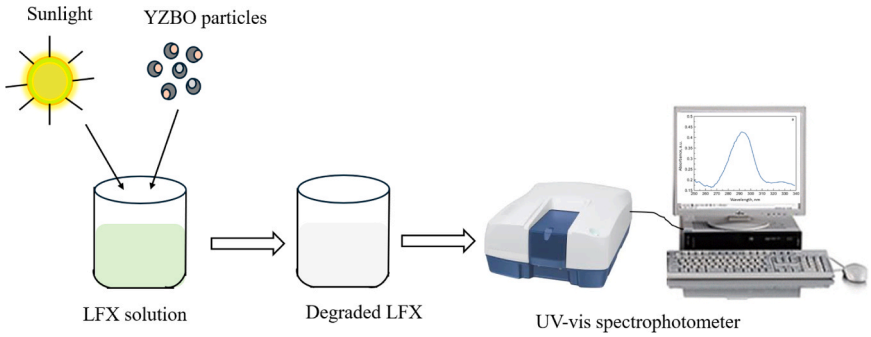

Fig. 2. Schematic diagram of photodegradation of LVF.

determined by using the same method for five cycles. The mineralization of LVF photodegraded by various YZBO photocatalysts under sunlight for 120 min was measured by a total organic carbon (TOC) analyzer (Model: TOC-$L_{CSH/CPH}$, Shimadzu Corporation, Japan).

3. Results and discussion

3.1. Structural analysis

The XRD analysis of the pure and Y-doped zinc bismuth oxide samples was performed for structural and phase analysis with a scanning speed of 0.012°/s in the 2θ range of 20.00 ° to 80.00 °. In Fig. 3(a), the XRD pattern of YZBO−0 showed the diffraction peaks at 2θ = 27.87,

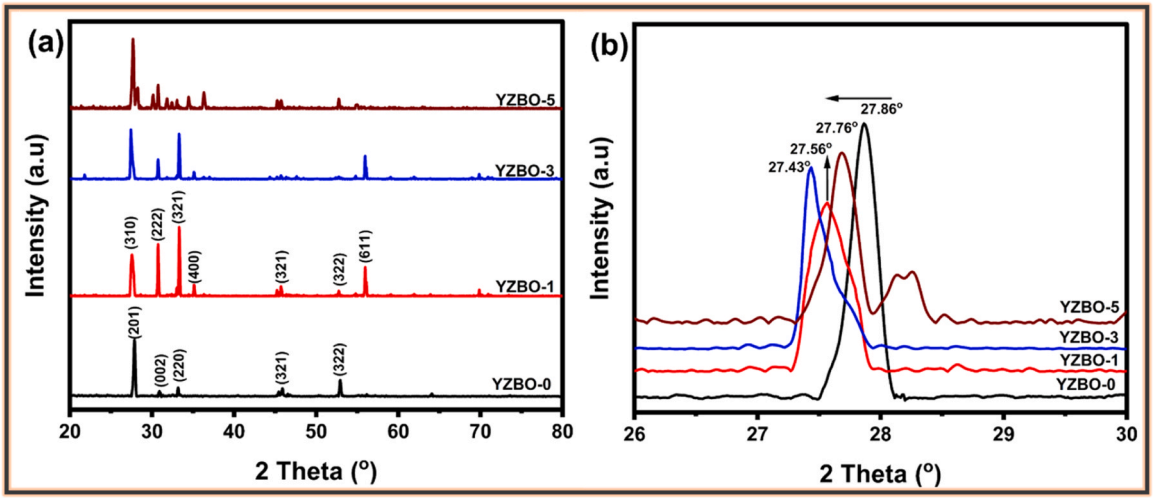

Fig. 3. XRD patterns of pure ZBO and Y-doped ZBOs (a), and shift of the major peak due to doping (b).

30.92, 33.17, 45.91, and 52.92 ° corresponding to the (201), (002), (220), (321), and (322) planes of the tetragonal crystal, which matched with JCPDs 00–043–0449. The observed peak shifts and changes in intensity observed for the Y-doped ZBOs (YZBO−1, YZBO−3, and YZBO−5) indicate lattice distortion induced by yttrium incorporation. The maximum shift of the major peak was observed for YZBO−3. These changes are attributed to differences in ionic radius and local structural rearrangements. Similar structural modifications have been reported in $ZnBi_2O_4$ and related spinel oxide systems in published articles, where doping and defect engineering induce lattice distortion and phase evolution [22]. In Fig. 3(b), a slight shift of the major peak toward lower 2θ values was observed compared with the pristine $ZnBi_2O_4$, indicating an expansion, which can be attributed to the doping of Y^{3+} ions. The system is then reorganized to reduce this strain, and this leads to stabilization of a more symmetric cubic phase. The observed structural and optical modifications may be associated with defect formation, including possible oxygen vacancies, which increase the phase change to transform the defect chemistry and lower the lattice energy. This kind of transformation increases charge carrier mobility and photocatalytic activity by inhibiting electron-hole recombination [29]. The structural parameters of YZBO−0 and doped materials were determined from the XRD data using the Scherrer formula and the Williamson–Hall method as given in Table 1. The broadening of diffraction peaks, Full Width at Half Maximum (FWHM), was analyzed to estimate the average crystallite size (D), microstrain (ε), and dislocation density (δ), which provide insight into the lattice distortion and crystallinity of the prepared samples. The narrower the FWHM, the larger the crystallite size and the fewer defects (higher crystallinity). On the other hand, the broader the FWHM, the smaller the crystallite size, the more strain or disorder. The average crystallite size was calculated using the Scherrer equation:

$$D = \frac{K\lambda}{\beta \cos\theta} \tag{1}$$

where D, K, λ, and β are the average crystallite size (nm), Scherrer constant, the X-ray wavelength, and FWHM, respectively. This equation allows the measurement of the apparent crystallite size, assuming that peak broadening originated primarily from small crystal domains. To distinguish between the effects of crystallite size and lattice strain on peak broadening, the Williamson-Hall (W-H) equation was applied:

$$\beta \cos\theta = \frac{K\lambda}{D} + 4\varepsilon \sin\theta \tag{2}$$

Here, the plot of $\beta cos\theta$ versus $4sin\theta$ gives a straight line, where the intercept corresponds to $K\lambda/D$ (used to calculate D), and the slope gives the microstrain (ε). The dislocation density, representing the amount of lattice imperfection, was estimated from the crystallite size using the relation:

$$\delta = \frac{1}{D^2} \tag{3}$$

The introduction of yttrium (Y^{3+}) into the zinc bismuthate ($ZnBi_2O_4$) lattice, typically forming a $ZnBi_{2-x}Y_xO_4$ (or similar) spinel structure, acts as a structural modifier by substituting for bismuth or zinc, resulting in modifications such as lattice distortion, alteration of crystallite size, and the creation of defects. The microstrain of Y-doped $ZnBi_2O_4$ dropped to near-zero for YZBO−1 and YZBO−3, indicating relaxation of lattices and passivation of defects. However, for YZBO−5, a weak positive strain has re-emerged because of the saturation of the dopant sites. The increase in microstrain observed after yttrium doping indicates the introduction of lattice distortion and local structural disorder, which may arise from differences in ionic size and local coordination environments. The density of dislocation is inversely proportional to the square size of crystallites, which reduces with a low degree of Y-doping, then increases with further increase of doping. The moderate crystallite size and a highly ordered, stress-free crystal lattice with high crystallinity and larger crystalline domains (YZBO−3) provide the most optimal structure towards photocatalytic activity. A minor secondary phase observed in the YZBO−5 sample may be attributed to excess yttrium incorporation, suggesting that higher doping levels approach the solubility limit within the $ZnBi_2O_4$ lattice. The calculated values of structural parameters of $ZnBi_2O_4$ with various levels of Y dopant are given in Table 1.

Table 1
Structural parameters such as Crystallite size, microstrain, and dislocation density, calculated using XRD data.

Parameters	YZBO−0	YZBO−1	YZBO−3	YZBO−5
Crystallite size (D) (nm)	43.32	41.08	51.49	54.29
Microstrain (ε) (με)	2.85×10^{-3}	4.79×10^{-3}	4.66×10^{-3}	4.64×10^{-3}
Dislocation density (δ) (nm^{-2})	0.00053	0.00059	0.00038	0.00034

The FTIR spectral analysis is a useful technique to determine the bond vibrations among the molecules, which confirms the successful synthesis of a material. The FTIR spectrum of ZBO (YZBO−0) shows a wide absorption band at 3450 cm^{-1} associated with the stretching vibrations of the O–H groups of water molecules adsorbed onto the surface of ZBO [30], as shown in Fig. 4(a). It also shows characteristic IR bands at 440, 548, 995, 1330, and 2950 cm^{-1}, and they are associated with ZnO of the tetrahedral (ZnO_4) units within the $ZnBi_2O_4$ catalyst structure, Bi–O bond vibrations, tetragonal spinel structure, impurities (e.g., NO_3^-/CO_3^{2-}), and C–H stretching vibrations of CH_3 or CH_2, respectively [31–33]. The weak band at around 2350 cm^{-1} can also be associated with atmospheric CO_2 [31]. On the other hand, YZBOs also show very similar IR bands at 424, 570, 1420, 2350, 2940, and 3410 cm^{-1}, but their position considerably changed, and the band intensity decreased with an increase in Y-doping, indicating Y-doping caused modification of the ZBO spinel structure, inducing lattice distortion. The IR band at 570 cm^{-1} of the spectrum of YZBO−1 almost disappeared with an increase in Y-doping. In the case of Y-doped $ZnBi_2O_4$, a new band was formed at 850–860 cm^{-1}, which can be attributed to the symmetric or asymmetric stretching vibrations of Bi–O–Bi bonds within the tetragonal structure of $ZnBi_2O_4$ [34]. The observed shifts in FTIR bands and changes in peak intensity suggest modifications in the local bonding environment following yttrium addition. These observations are consistent with structural changes induced by doping. However, FTIR alone cannot provide direct confirmation of yttrium incorporation into the $ZnBi_2O_4$ lattice.

The Raman spectroscopic analysis was utilized to explain the structural characteristics and phase evolution of pure $ZnBi_2O_4$ and Y^{3+}-doped $ZnBi_2O_4$ [35,36]. The Raman spectra of ZBO and YZBOs are presented in Fig. 4(b). While Raman spectra for pure ZBO can feature multiple peaks between 100 and 1000 cm^{-1}, the characteristic of the crystalline lattice vibrational mode in the stoichiometric $ZnBi_2O_4$ material and the vibrational mode of the Bi-O bonds can be clearly observed at 123 and 160 cm^{-1} [35]. On the other hand, Y-doped $ZnBi_2O_4$ (YZBOs) show new bands at 354 and 458 cm^{-1} with high intensity, which are generally associated with the low-frequency lattice vibrations or internal bending modes, and vibrational modes of Y–O within the tetragonal structure of ZBO, respectively, suggesting some Bi ions were replaced with Y ions and became part of ZBO [36,37]. 1 and 5 mol% Y-doping produced wider and low–intensity Y–O bands, causing substantial distortion of the ZBO structure and creating defects. 3 mol% Y-doping caused the Y–O bond-associated bands to narrow along with a substantial increase in FWHM, suggesting less lattice distortion, higher crystallinity, and efficient charge separation at the interface compared to other YZBOs.

3.2. Optical properties

Direct migration of an electron in the valence band (VB) to the conduction band (CB) is most visually represented by absorption bands. The band gap between valence and conduction bands was measured

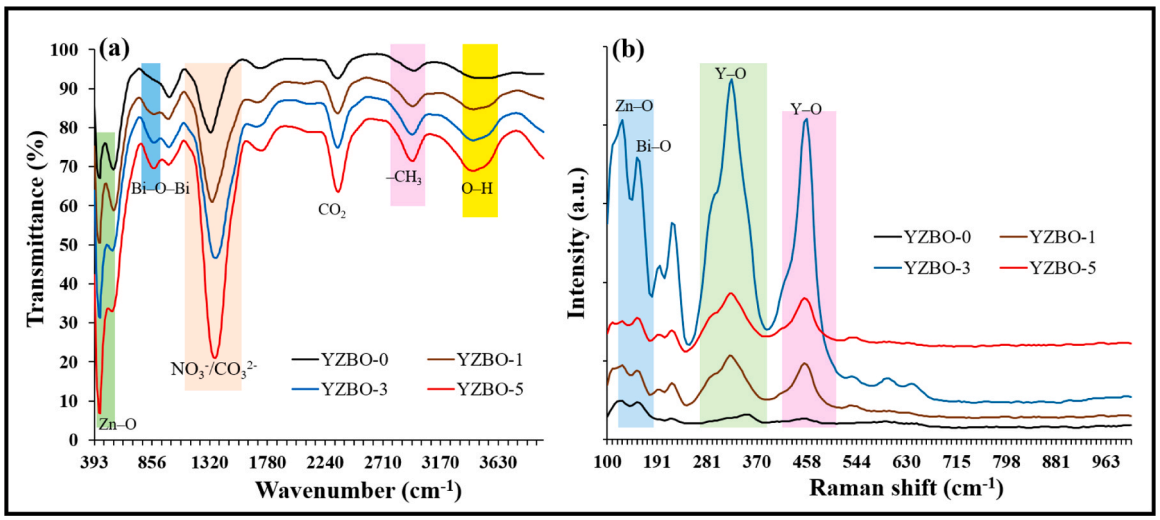

Fig. 4. FTIR (a) and Raman (b) spectra of pure and Y-doped $ZnBi_2O_4$ (YZBO−0, YZBO−1, YZBO−3, and YZBO−5) showing characteristic vibrational bands corresponding to metal–oxygen bonding and doping of yttrium, respectively.

using UV–vis spectroscopy in the range of 200–800 nm wavelength. Further, the influence of the doping of Y on the $ZnBi_2O_4$ on the optical band gap was observed by absorption spectra. Fig. 5(a) illustrates the UV-Vis absorbance spectra of YZBO−1, YZBO−3, and YZBO−5, which showed absorption in the visible as well as the UV region, and a maximum absorption was noted in the range of 250–400 nm. However, a red shift (or bathochromic shift) of the absorbance peak was observed towards the visible light wavelength of the electromagnetic spectrum for the UV–visible spectrum of the 3% Y-doped $ZnBi_2O_4$. It indicates that the 3% Y-doped $ZnBi_2O_4$ molecules are absorbing light at a lower energy

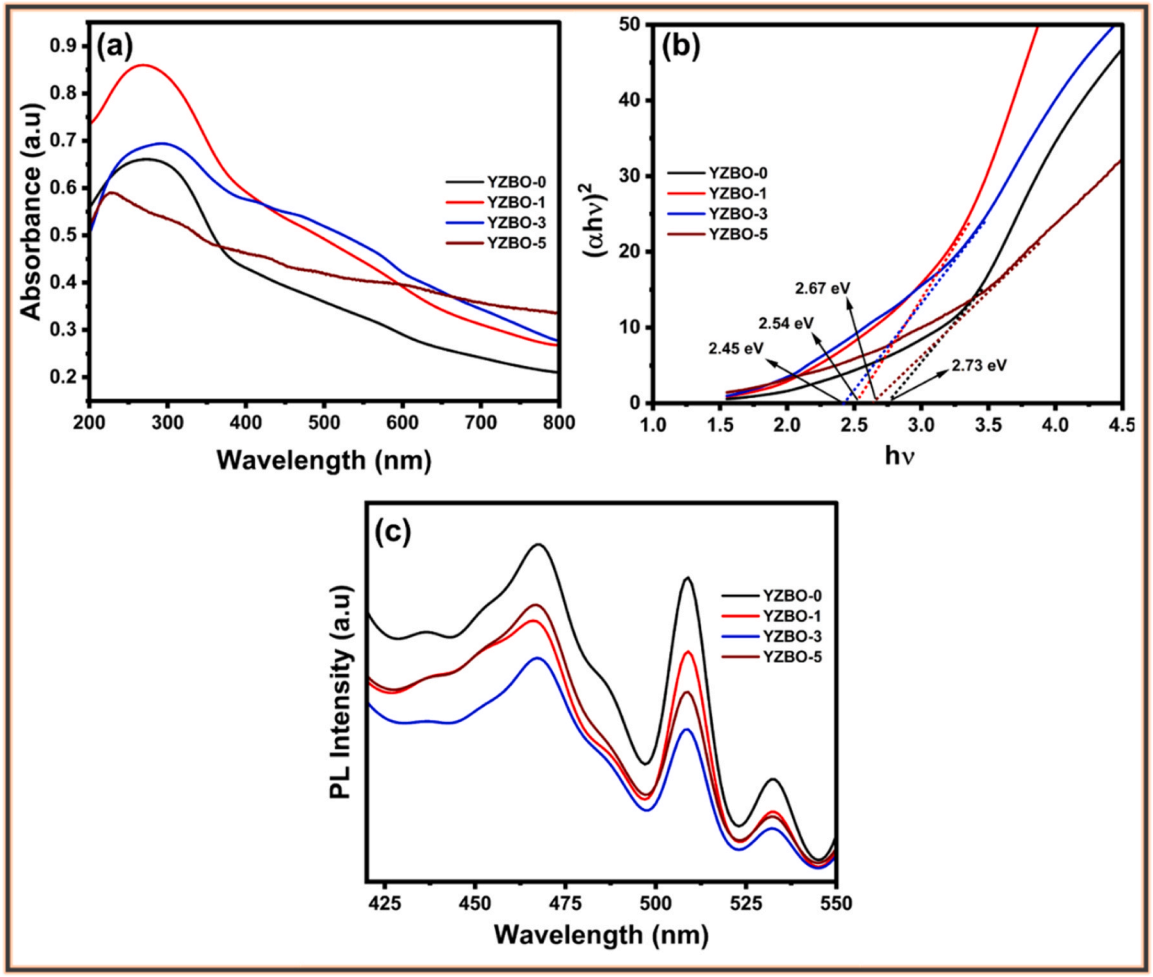

Fig. 5. UV-Visible spectra (a), Tauc's plot (b), and PL spectra (c) of synthesized YZBO−0, YZBO−1, YZBO−3, and YZBO−5 photocatalysts.

frequency compared to the undoped $ZnBi_2O_4$, suggesting the reduction of its bandgap and enhancing its visible-light absorption capability [38]. The UV–vis absorption spectra of the doped spinel oxide samples revealed that when the concentration of the dopant increases, the absorption capacity of the photocatalyst may decrease. This gives insight into efficient light-harvesting for 3% Y-doped $ZnBi_2O_4$. The YZBO−0, YZBO−1, YZBO−3, and YZBO−5 exhibit a direct band gap of 2.73, 2.67, 2.45, and 2.54 eV, respectively. The observed reduction in band gap upon yttrium doping can be

attributed to the introduction of defect states and oxygen vacancies within the band structure. The fact that 3% Y doping leads to a reduced band gap, and the reduction in bandgap energy observed after yttrium doping may be associated with modifications in the electronic structure and the possible introduction of defect-related states. The optical band gap was estimated using Tauc's method, assuming a direct allowed transition, which has been common for $ZnBi_2O_4$ and related spinel oxides. The linear extrapolation of $(\alpha h\nu)^2$ versus $h\nu$ was used to determine the band gap energy.

$$\alpha h\nu = A(h\nu - E_g)^n \quad (4)$$

A is the proportionality constant, n is the photon frequency, which is 2 for a direct band gap, and α is the absorption coefficient. Many studies have shown solid evidence of the reduction of the band gap energy with an increase in the doping concentration up to a specified limit [39]. After calculating the band gap (E_g) of Y-doped and undoped $ZnBi_2O_4$ using Tauc's plot from the intercept of the $(\alpha_{hv})^2$ vs hv curve presented in Fig. 5(b), we estimated the valence band (E_{VB}) and conduction Band (E_{CB}) edge positions using the Mulliken electronegativity and band gap data from the following formulas [40]:

$$E_{CB} = \chi - 0.5E_g \quad (5)$$

$$E_{VB} = E_{CB} + E_g \quad (6)$$

The band gap energy of the as-synthesized material was determined by using Tauc's plot, as shown in Fig. 5(b).

The structure of a material has a significant impact on its optical properties, which explains the photocatalytic properties of the material due to its charge carrier transport efficiency. The efficiency of electron-hole pair separation can be estimated by photoluminescence spectroscopy (PL) [41]. The PL emission intensity is directly related to charge separation; larger PL peak intensities represent a decrease in charge separation efficiency, and lower peak intensity indicates the enlarged lifetime of charge separation. A high PL intensity indicates that a large amount of charge carriers is recombining unproductively, leading to poor catalytic performance, and a lower PL intensity indicates greater suppression of electron-hole recombination, leading to improved catalytic performance. As shown in Fig. 5(c), the 3% Y-doped $ZnBi_2O_4$ sample (YZBO−3) exhibited the lowest PL intensity, while the pure $ZnBi_2O_4$ material had the highest PL intensity. This suggests that rare earth ions improve the spatial charge separation efficiency through interfacial dipole interactions. The lower PL intensity observed for YZBO−3 suggests a reduction in the recombination probability of photogenerated charge carriers. However, it should be noted that PL analysis provides qualitative insight, and further time-resolved or quantitative studies would be required for precise evaluation of charge carrier dynamics. These optical characteristics, including band gap reduction and suppressed recombination, collectively contribute to the enhanced photocatalytic performance of the Y-doped $ZnBi_2O_4$ samples.

3.3. Morphological analysis

Surface morphologies of pure and Y-doped $ZnBi_2O_4$ (YZBO−1, YZBO−3, and YZBO−5) were examined by scanning electron

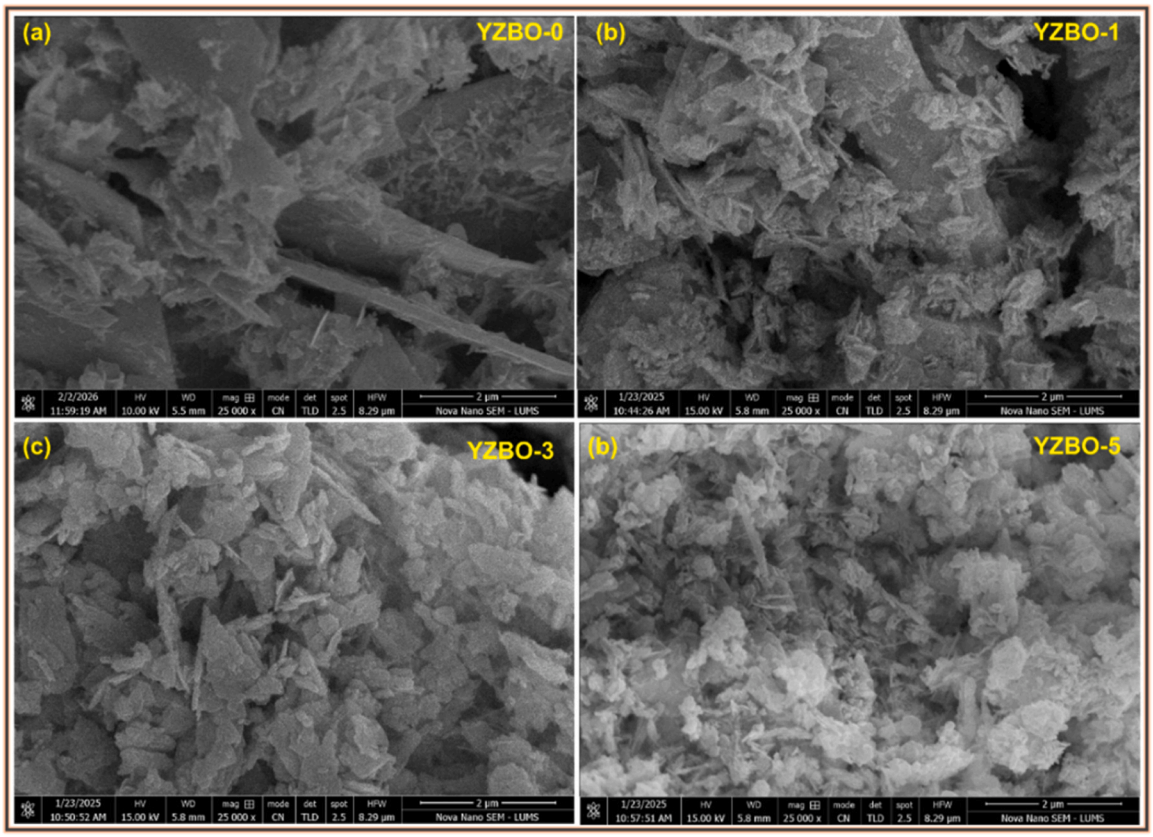

Fig. 6. SEM images illustrating the surface morphology of pure and Y-doped $ZnBi_2O_4$ (YZBO−0, YZBO−1, YZBO−3, and YZBO−5), highlighting the evolution of nanosheet structures with varying Y doping concentrations.

microscopy, which is presented in Fig. 6. The SEM image of pure $ZnBi_2O_4$ showed a sheet-like morphology, while Y-doped $ZnBi_2O_4$ showed an agglomerated particle structure with irregularly shaped particles. The sheets are closely piled up, and this

makes the inter-particle voids not so big. This type of compact morphology inhibits surface area as well as the availability of active sites and may limit the efficient adsorption of pollutants and accessibility of photocatalytic light during photocatalysis. The SEM image of YZBO−3 exhibits a clearly defined, homogeneous, and highly porous sheet-like morphology. The nanosheets are seen to be thinner and more uniformly dispersed and in a loosely packed structure, which provides more roughness and exposes more reactive facets. The photocatalytic activity of such a network is extremely useful since it is an open and interconnected network that enhances the efficiency of charge separation and diffusion of reactants and photons. For the photocatalyst YZBO−5, morphology is more disordered and aggregated than that of YZBO−3. Y seems to promote the aggregation of particles on over-doping, which results in low porosity and a lack of available active sites. SEM analysis reveals morphological variations upon yttrium doping; however, these observations provide qualitative insight only. The relationship between morphology and photocatalytic performance is indirect and should be interpreted in conjunction with other characterization techniques.

The elemental composition of ZBO and Y-doped $ZnBi_2O_4$ was analyzed by EDX spectroscopy, as presented in Fig. 7 (a-d). In all the samples, there were high peaks of Bi, Zn, and O, which proved that the formation of the $ZnBi_2O_4$ matrix had occurred. Each spectrum contained a weak, although distinct, Y signal (its intensity increased with an increase in Y%), which confirms the presence of yttrium along with Zn, Bi, and O; however, it does not provide direct evidence of its incorporation into the crystal lattice. In comparison, YZBO−1 exhibited comparatively decreased Y incorporation, and YZBO−5 had a better Bi signal with a minor decrease in Zn intensity, which indicates that there might be surface segregation or structural abnormality at the higher level of dopant. EDX analysis confirms the presence of Zn, Bi, O, and Y elements in the synthesized samples. The detection of yttrium indicates its successful introduction during synthesis; however, EDX alone cannot determine the exact location, distribution, or incorporation mechanism of the dopant within the crystal lattice.

The textural properties of the most active material, YZBO−3, by nitrogen adsorption-desorption isotherm based on Brunauer-Emmett-Teller (BET), provide insights about the presence of a Type IV profile. A distinct hysteresis loop in the higher relative pressure confirms the formation of mesoporous material. The smaller hysteresis gap between adsorption and desorption further confirms the formation of well-defined mesoporous material with a uniform pore diameter. In Fig. 8, the obtained BET specific surface area was 8.80 m^2/g, while the single point surface area was 7.81 m^2/g. However, a relatively higher surface area, 16.18 m^2/g, was found by the Langmuir adsorption model, which may be due to the formation of a monolayer on a homogeneous surface. The pore volume was calculated using the Barrett–Joyner–Halenda (BJH) method, and the total pore volume for YZBO−3 was 0.0552 cm^3 / g. The adsorption pore volume of 0.0564 $cm^3\ g^{-1}$ and desorption pore volume 0.0574 cm^3 /g confirm the formation of a well-defined and stable pore structure. The average hole diameter obtained by the BET method is 25.09 nm, whereas 16.22–16.91 nm was calculated by the BJH method, confirming the formation of mesoporous material with an open pore network, which can be helpful for diffusion and the usability of active sites.

3.4. *Photocatalytic performance*

The degradation of LVF (5 ppm) was conducted for the Y-doped $ZnBi_2O_4$ nanomaterials under sunlight at a catalyst dose of 0.4 g/L to assess the photocatalytic performance of the synthesized undoped and doped $ZnBi_2O_4$. The time-dependent UV–visible absorption spectra presented in Fig. 9(a) show a gradual decrease in absorption peaks associated with LVF with an increase in the solar irradiation time, confirming the increase in degradation of LVF by various Y-doped $ZnBi_2O_4$ with time. The results suggest that the photocatalyst with 3% dopant (YZBO−3) exhibited the highest degradation of LVF and the best photocatalytic performance. The degradation of LVF reached 98.5% after 120 min of solar irradiation, which is considerably higher than the LVF photodegradation shown by 3% europium-doped $ZnBi_2O_4$, which is 93.4% [22]. As expected, the undoped $ZnBi_2O_4$ showed only 70.6% degradation of LVF. A suitable concentration of the dopant enhanced photocatalytic activity, which may be attributed to doping-induced

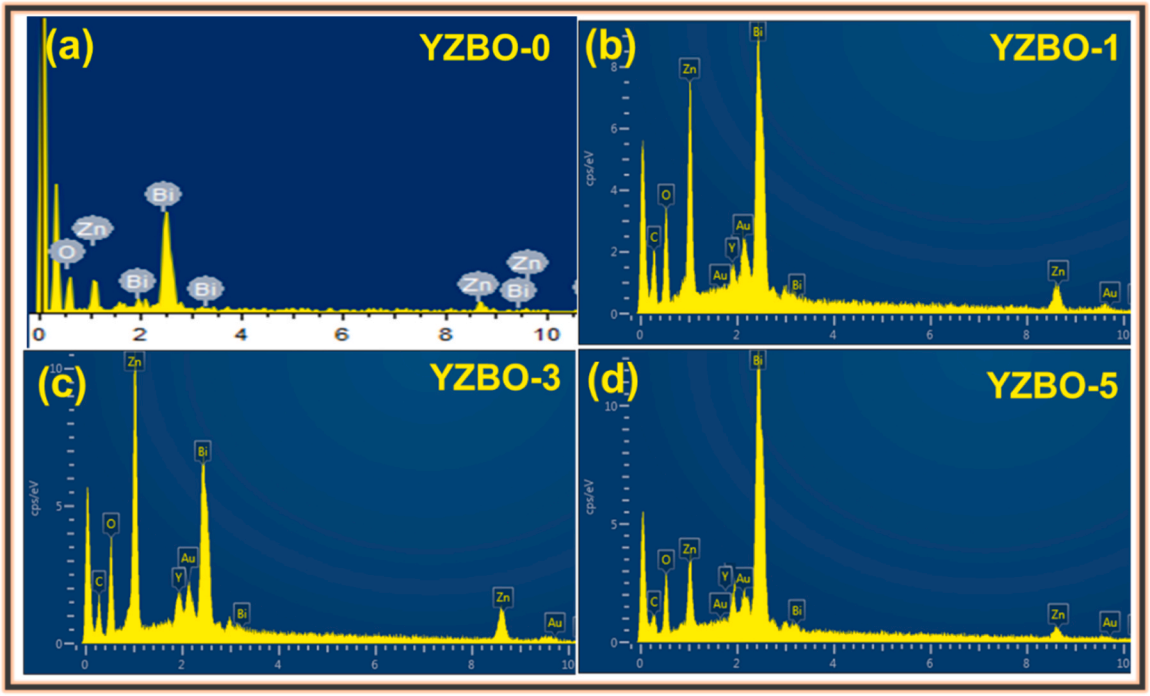

Fig. 7. EDX spectra of YZBO−0, YZBO−1, YZBO−3, and YZBO−5 to confirm their elemental compositions.

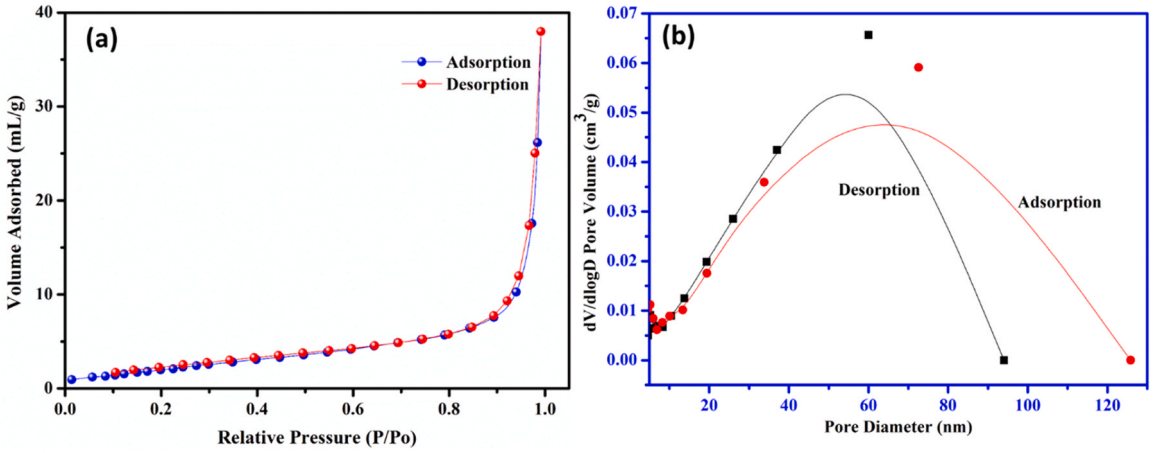

Fig. 8. BET surface area (a) and BJH pore size distribution (b) of YZBO−3.

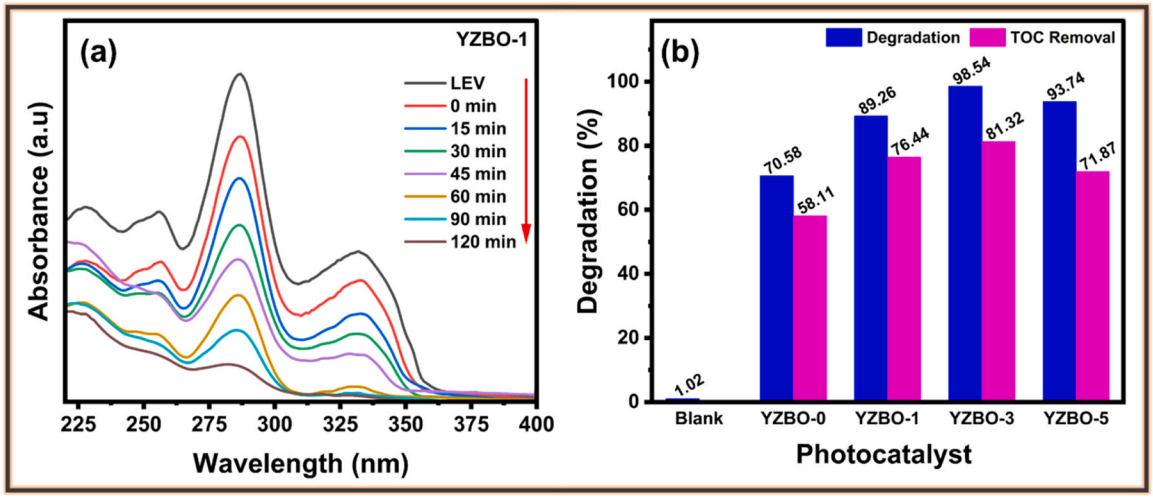

Fig. 9. Time-dependent photocatalytic degradation of LVF by YZBO−1 (a), and LVF degradation efficiency of YZBO with 0, 1, 3, and 5% Y-doping (b).

modifications in the host material, which can efficiently enhance the separation of photogenerated carriers and give more reactive sites. Moreover, the influence of the photocatalysts of various Y doping levels on the efficiency of LVF degradation was presented in Fig. 9(b). This is because a sufficient concentration of Y doping can add extra energy levels and change the electron transport mechanism. YZBO−3 showed the highest degradation performance, as 3 mol% Y caused the highest disruption in the ZBO structure and increased. Hence, suppress the enhancements of photocatalytic activity, which can be clearly observed with 5% doping (93.7%). The pure YZBO−0 showed only 70.6% degradation, while YZBO−1 exhibited 89.3% degradation after 120 min. The optimal 3% doping demonstrates nearly complete removal of LVF, showing the best photocatalytic activity.

TOC analysis was performed to evaluate the extent of mineralization of LVF. Fig. 9(b) shows the TOC reduction of LVF by various YZBO photocatalysts, which is a direct indicator of mineralization; i.e., the higher the TOC reduction, the higher the mineralization of LVF. The results clearly show that the Y-doping into YZBO increased its TOC reduction efficiency. The undoped YZBO showed only 58.1% TOC reduction, but YZBO with 1% Y doping (YZBO−1) exhibited 76.4% TOC reduction, i.e., a 31.5% increase in TOC reduction, which is quite significant. The highest TOC removal was exhibited by YZBO−3, which was 81.3%, i.e., the increase in TOC reduction by YZBO−3 was 39.3%.

3.5. Kinetic study

The pseudo-first-order model was selected because it provided a satisfactory fit to the experimental data and is commonly applied in photocatalytic degradation studies. Nevertheless, the evaluation of alternative kinetic models may provide additional mechanistic insight and should be considered in future investigations. The degradation kinetics were analyzed using a pseudo-first-order model, expressed as Eq. (7):

$$-\ln(C/C_0) = Kt \quad (7)$$

where C_0 and C represent the initial and time-dependent concentrations of LVF, respectively, and k is the apparent rate constant. The rate constants were obtained from the slope of the linear regression plots of $\ln(C_0/C)$ versus time. The photocatalytic degradation of LVF using Y-doped ZBO was studied using kinetic analysis as shown in Fig. 10(a-c). The reaction followed pseudo-first-order kinetics, as confirmed by high R2 values of 0.97–0.99. It should be noted that the pseudo-first-order model provides an empirical approximation of the degradation kinetics and does not necessarily represent the true reaction mechanism. As shown in Fig. 10(d), the rate constant of pure YZBO−0 was 0.0091 min^{-1}, which increased to 0.0168 min^{-1} for the YZBO−1 photocatalyst. The maximum rate constant (0.0345 min^{-1}) was exhibited by YZBO−3 but further increase in Y-doping reduced the rate constant to 0.0210 min^{-1}. The best performance was exhibited by the 3% doped

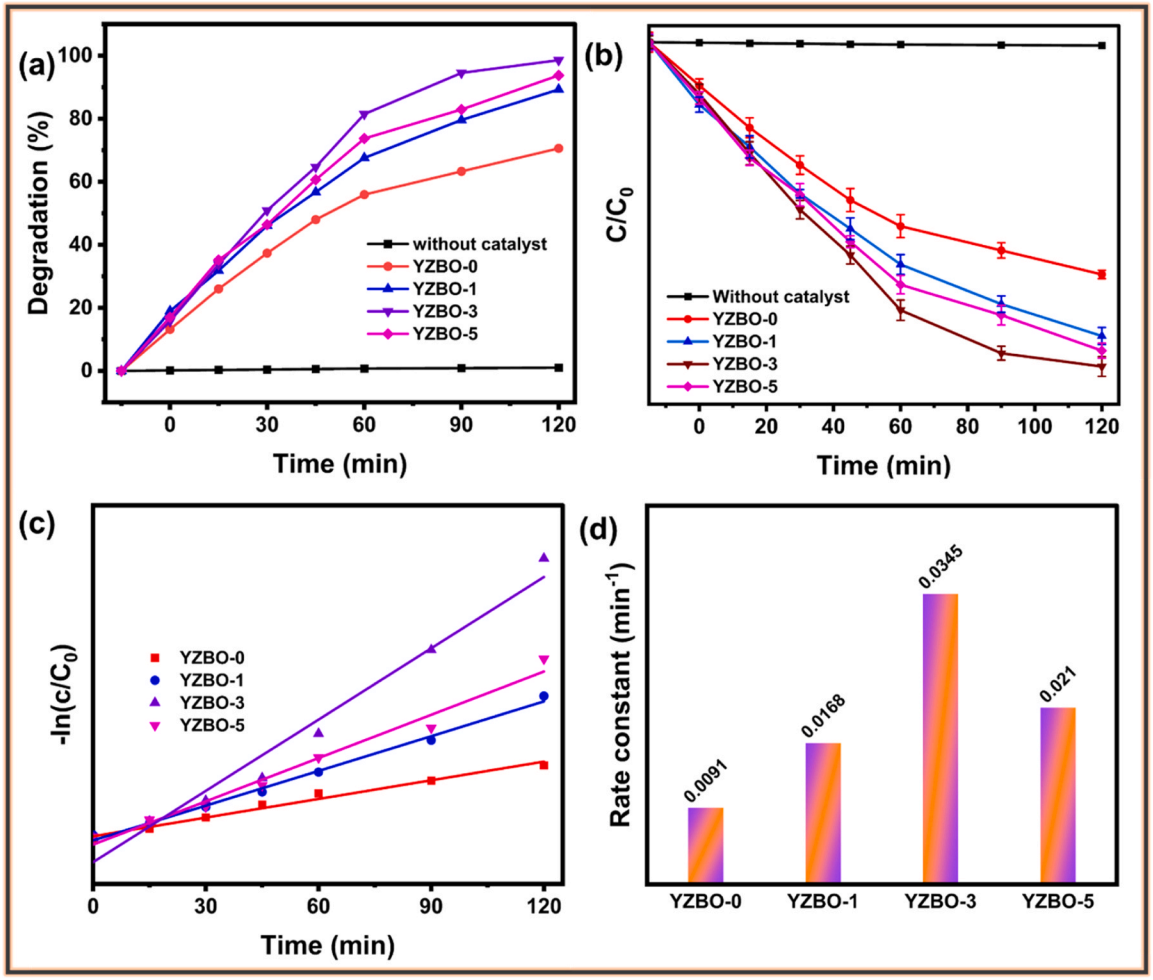

Fig. 10. Pseudo first-order kinetic study (a-c) and rate constant evaluation (d) of LVF degradation by various photocatalysts.

$ZnBi_2O_4$. At the optimal doping concentration of 3%, lattice distortion narrows the band gap to 2.45 eV (UV–Vis), enhancing visible-light absorption. The enhanced rate constant observed for YZBO−3 may be associated with improved charge-carrier utilization and favorable structural and optical characteristics; however, direct confirmation would require complementary electrochemical and time-resolved spectroscopic analyses. In contrast, 1% doping is inadequate for effective band gap modulation, while 5% doping introduces excessive disorder that widens the band gap. Thus, both lower and higher doping levels are unfavorable for optimal band gap tuning, consistent with the findings of others for the W-doped CuS systems [42]. This shows that at this level, yttrium-doping provides the most efficient separation of charges and more active sites for LVF degradation. The enhanced rate constant observed for YZBO−3 may be associated with improved charge-carrier utilization and favorable structural and optical characteristics; however, direct confirmation would require complementary electrochemical and time-resolved spectroscopic analyses.

The enhanced kinetic performance of YZBO−3 may be attributed to improved charge separation and increased availability of active sites; however, these interpretations remain qualitative in the absence of direct electrochemical or time-resolved measurements. At 3% doping, the system generates beneficial shallow trap states (oxygen vacancies) that effectively suppress electron–hole recombination, consistent with the lowest PL intensity. In contrast, 5% doping exceeds the solubility limit, inducing deep trap states that act as recombination centers and degrade charge separation. A similar optimal charge separation followed by structural deterioration at higher doping has been reported by Elhadi et al. for the Sr-doped $NiFe_2O_4$ [43]. At 3% doping, dopant incorporation effectively inhibits crystal growth, promoting the formation of porous nanosheet structures with enhanced surface area (SEM/BET). In contrast, 5% doping induces particle agglomeration due to excessive surface dopants blocking active sites and reducing surface accessibility. The enhanced kinetic performance of YZBO−3 is also related to its structural and optical characteristics, such as lattice distortion (XRD), decreased band gap (UV-Vis), suppressed recombination (PL), and increased surface area (BET), which can be seen to help in achieving more efficient photocatalytic activity.

3.6. *Optimization of drug concentration and dose of catalyst*

3.6.1. *Effect of LVF concentration*

The effect of an increase in LVF concentration on the photocatalytic degradation efficiency of LVF by the YZBO−3 photocatalyst is presented in Fig. 11(a). As expected, the degradation of LVF decreased from 97.4% to 74.8% with an increase in LVF concentration from 2.5 to 10.0 ppm within 120 min of sunlight irradiation. The higher initial LVF concentration showed a negative impact on the photocatalytic degradation of LVF, primarily because it caused active site saturation on the catalyst surface, light shielding (screening) effects, and radical scavenging. As the number of LVF molecules increases, they outnumber the available surface sites of the photocatalyst where degradation occurs, leading to a decrease in the overall degradation efficiency. The increase in the LVF concentration increased the turbidity of the LVF solution, and possibly LVF molecules themselves absorbed or scattered the incident sunlight, obstructing the photons of light from reaching the catalyst surface, resulting in a decrease in the production of •OH and $\bullet O_2^-$ radicals,

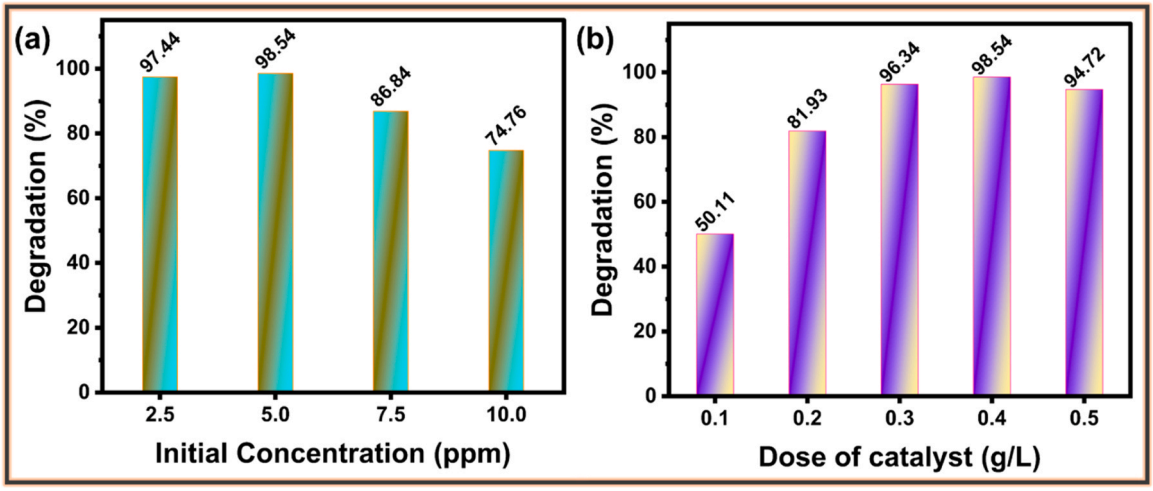

Fig. 11. Effect of initial concentration of LVF (a) and YZBO−3 dosage (b) on the degradation efficiency of LVF.

reducing the degradation of LVF. Moreover, increasing the concentration of LVF produced intermediate degradation products, which might be adsorbed onto the catalyst surface, causing surface fouling of the catalyst and blocking further degradation. Considering the photodegradation results, 5.0 ppm was found to be the optimum concentration, which provided the highest degradation efficiency (98.5%). These results suggest that a very high LVF concentration is not favorable for maximizing LVF degradation.

3.6.2. *Effect of catalyst dose*

The effect of catalyst dose on the degradation of LVF was investigated using YZBO−3 at five different doses, 0.1, 0.2, 0.3, and 0.4 g/L. The results are shown in Fig. 11(b), which shows that the degradation efficiency of LVF improved with an increase in the catalyst dose. Increasing the dose of catalysts results in a higher number of active sites and a higher density of catalyst particles in the illuminated area. Therefore, the photocatalytic capacity of the material is improved, resulting in faster decomposition [44]. However, if the catalyst content is continuously increased, it may lead to an excessive density of particles suspended in solution, which hinders light penetration and promotes the light scattering effect by preventing light absorption during the reaction, resulting in a decrease in catalytic activity. Consequently, further increasing the catalyst dosage (0.5 g/L) did not lead to an improvement in photocatalytic performance. Therefore, a dose of 0.4 g/L was optimal for the photodegradation of LVF in 120 min.

3.6.3. *Influence of initial pH of drug solution*

The initial pH value of the LVF solution plays a crucial role in activating the photocatalyst. In this study, the effects of initial pH on the photodegradation of LVF over Y-doped $ZnBi_2O_4$ in Fig. 12(a-b) were investigated from pH 3–11. As shown in Fig. 12(a), the degradation efficiency was highly dependent on the solution pH. At pH 3, only **40.1%** degradation of LVF was observed, which gradually increased to 79.0% at pH 5. A significant improvement was achieved in the neutral range, where the maximum degradation of 98.5% was achieved at pH 7. The improved performance observed at this pH may be associated with favorable interactions between the catalyst surface and levofloxacin species present under the experimental conditions; however, direct surface-charge measurements were not performed. A slight decrease was noted at pH 9, and a sharper drop occurred at pH 11. These results clearly indicate that neutral to weakly alkaline conditions are the most favorable for LVF degradation. Fig. 12(b) revealed that the point of zero charge (pH_{pzc}) of the catalyst is around 7.8. Below this value, the photocatalyst surface is positively charged, and it becomes negatively charged above pH 7.8. It is known that, as an amphoteric compound, LVF has two dissociation constants, 5.6–5.8 (pK_{a1}) and 7.9–8.7 (pK_{a2}), due to the presence of both an acidic and a basic functional group. This means that the surface of LVF molecules is cationic below pH 5.6,

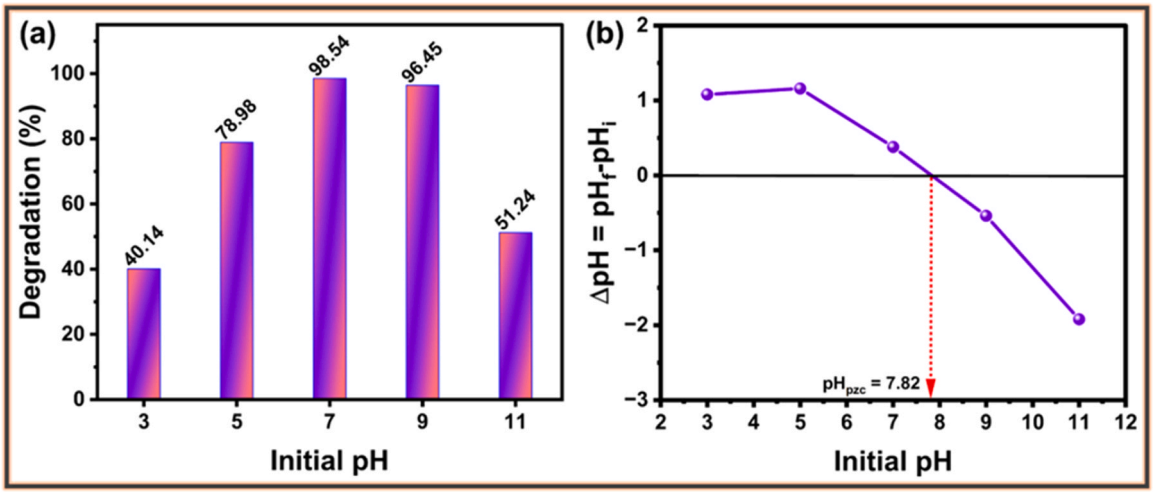

Fig. 12. Effect of initial pH (a) on degradation efficiency and the optimized pH condition (b) for LVF degradation.

anionic above pH 7.9, and neutral between pH 5.6 and 7.9 (Fig. 12b). On the other hand, the pH_{pzc} of $ZnBi_2O_4$ is reported to be pH 7.8, i.e., the surface of the photocatalyst becomes positive below pH 7.8 and negative above pH 7.8 [45]. Hence, the electrostatic repulsion between LVF and YZBO−3 was high at pH levels below 7 and above 7, causing very low adsorption of LVF onto the YZBO−3 surface under those conditions due to their similar charge characteristics, resulting in poor degradation of LVF. On the other hand, the electrostatic repulsion between the surface of LVF and YZBO−3 was the minimum at neutral pH, causing the maximum adsorption of the LVF onto the catalyst surface, allowing the attack of LV molecules by the active species of the catalysts, resulting in the highest degradation of the LVF. Therefore, the maximum degradation of LVF occurred at pH 7.0, and it is the optimum pH for the photocatalytic degradation of LVF by YZBO−3 [46]. The influence of pH on photocatalytic activity may be explained by the variation of the surface charge of the catalyst and the ionization state of LVF, which determine adsorption and reaction efficiency.

3.6.4. Scavenging analysis

The proposed mechanism is based on indirect experimental evidence obtained from scavenger and optical studies. The study of the effect of various radical scavengers on the photocatalytic degradation of LVF can identify the primary active species involved in its photodegradation reaction with Y-doped $ZnBi_2O_4$ and help to understand the degradation mechanisms [47]. Typically, scavengers for hydroxyl radicals (•OH), superoxide radicals ($\bullet O_2^-$), and photogenerated holes (h^+) are used to selectively suppress the reactive species involved in the degradation process. In this work, isopropyl alcohol (IPA), silver nitrate ($AgNO_3$), EDTA, and para-benzoquinone (p-BQ) were used to scavenge the •OH, $\bullet O_2^-$, electrons (e^-), and h^+, and the results are presented in Fig. 13(a).

The photodegradation efficiency of LVF by YZBO−3 was 98.5% without the presence of any scavengers. However, the presence of various scavengers showed a significant effect on the photodegradation performance, negatively affecting the degradation efficiency. A moderate decrease in the degradation efficiency occurred in the case of $AgNO_3$ and EDTA, which inhibited the e^-/h^+ pairs and decreased the degradation efficiency from 98.5% to 81.6% and 92.8%, respectively. In contrast, the presence of IPA and p-BQ had a significant effect on the photodegradation process and reduced the degradation efficiency from 98.5% to 35.4 and 43.8%, respectively. The maximum reduction in degradation efficiency occurred when IPA was used as a scavenger. These results indicate that hydroxyl radicals and superoxide radicals play the primary role in the photodegradation of LVF by YZBO−3, and photogenerated charge carriers (e^-/h^+) also play a role in the degradation process. The presence of certain scavengers that inhibit photocatalytic activity also indicates the mechanism behind the photodegradation. Fig. 13(b) shows the active part of OH and $\bullet O_2^-$ in the degradation of LVF on the surface of photocatalyst YZBO−3 under sunlight irradiation. The improved performance observed at this pH may be associated with favorable interactions between the catalyst surface and levofloxacin species present under the experimental conditions; however, direct surface-charge measurements were not performed.

3.7. Reusability

To determine the stability and the durability of the Y-doped $ZnBi_2O_4$ nanoparticles, reusability experiments were conducted during five successive photocatalytic cycles in total, as shown in Fig. 14. The photocatalyst was recovered, washed, and reused after every cycle under the same conditions. The degradation percentage was also extremely high in all experiments, with only a minor difference, which showed that the photocatalyst is highly stable and recyclable. The degradation efficiency of LVF was 98.5, 97.2, 95.9, 94.5, and 94.2% in the 1st, 2nd, 3rd, 4th, and 5th cycles, respectively. The photocatalytic efficiency was slightly reduced with an increase in the number of recycles., which can be explained by the possibility that part of the catalyst could be

lost after each cycle of recovery and purification by washing, fouling of the surface by the adsorption of intermediates formed by the degradation of LVF, or even slight structural or active site inactivation due to long contact with light. However, confirmation would require further post-reaction characterization. Only a 4.4% reduction in photocatalytic performance was observed after five cycles of reuse, which is quite impressive. Nevertheless, the activity of the catalyst remained more than 95.6% of its original photocatalytic performance after five cycles of reuse, which shows a great level of stability, high structural integrity, and immense potential for practical wastewater treatment processes. To further investigate the structural and morphological stability of the photocatalyst after repeated use, additional characterizations were performed on the used YZBO−3 sample after five photocatalytic cycles. The XRD pattern of the reused photocatalyst showed no significant change in peak positions as compared to the fresh material, indicating that the crystal structure remained intact during the photocatalytic process. This confirms the high structural stability of the synthesized material. SEM analysis of the reused sample reveals that the nanosheet morphology is largely preserved, with only minor aggregation observed. These results confirm the structural and morphological stability of the photocatalyst after repeated use.

4. Outlook

This article demonstrates that Y-doped $ZnBi_2O_4$ can be used for the photocatalytic degradation of LVF under sunlight, which not only

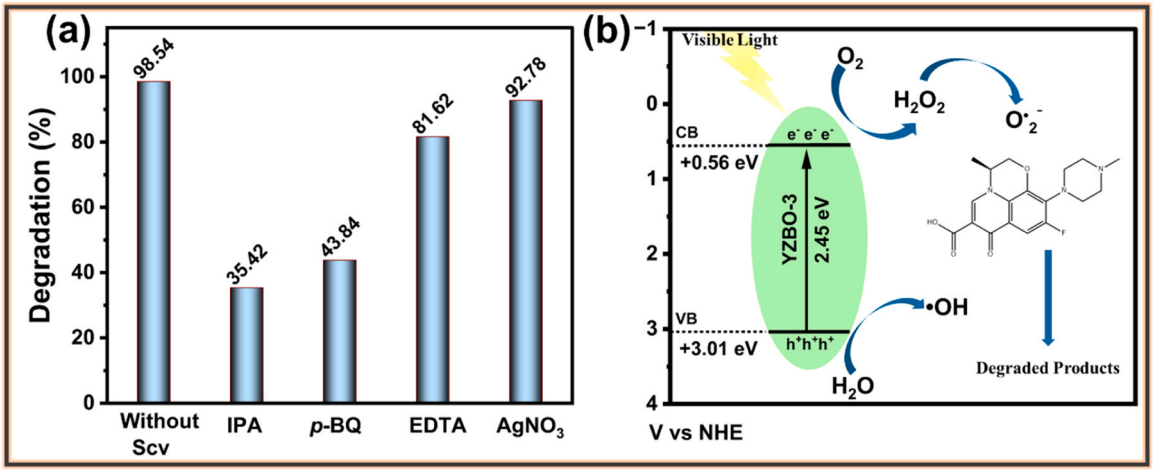

Fig. 13. Effect of radical scavenger (a) on photocatalytic degradation of LVF and reaction mechanism (b) at the surface of photocatalyst.

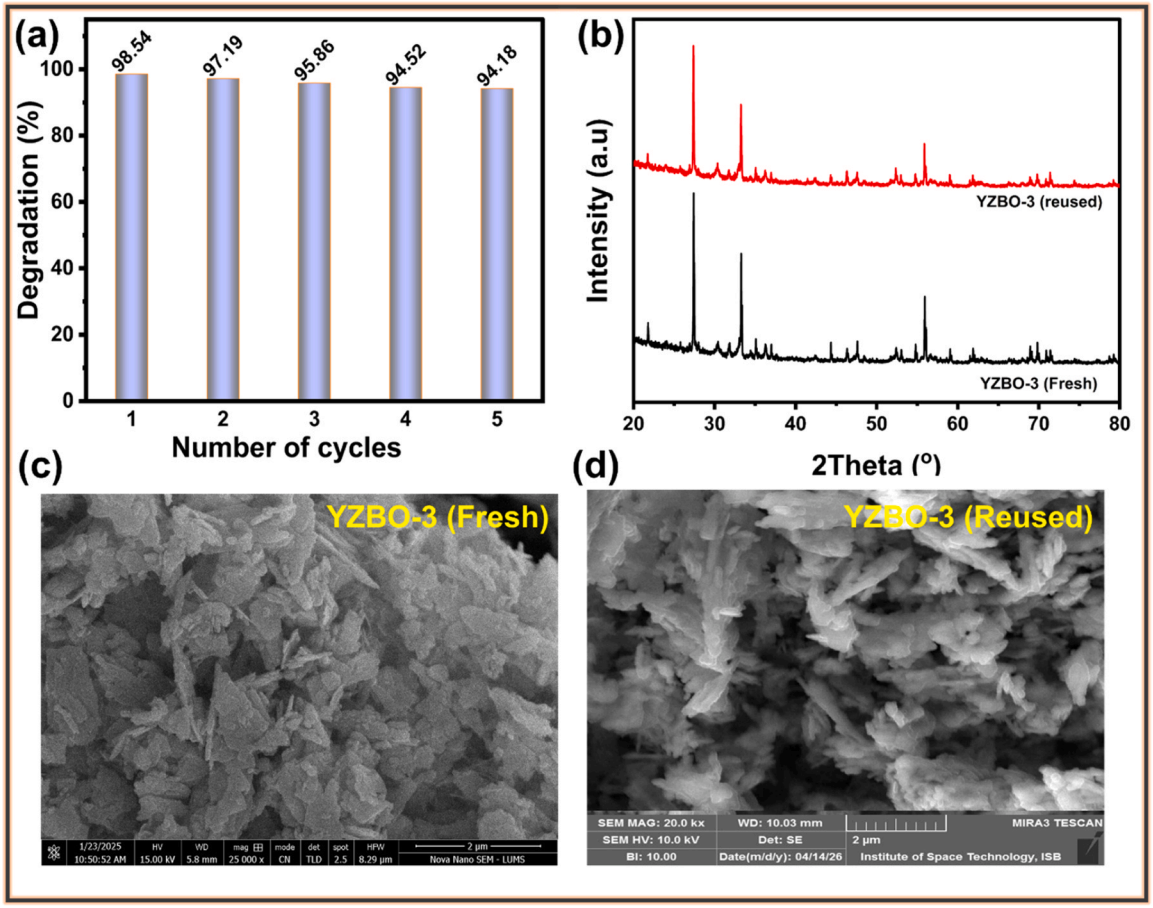

Fig. 14. Reusability tests of YZBO−3 photocatalyst for five cycles (b) XRD patterns of YZBO−3 before and after use, (c) SEM image of YZBO−3 (Fresh sample), and (d) SEM image of YZBO−3 (Reused sample).

exhibits excellent degradation of LVF within 120 min but also excellent TOC reduction. Many photocatalysts may show high degradation efficiency of pharmaceutical drugs, but they may show low TOC reduction, suggesting incomplete degradation of drugs. However, visible-light photocatalysts have several limitations that need to be considered, such as seasonal variations in solar intensity, atmospheric temperature, and spectral distribution of solar irradiation that may affect the performance of photocatalysts. In this work, all photocatalytic degradations were conducted under sunlight, but their long-term performance needs to be evaluated for practical applications.

Sunlight-based photocatalysts are a promising, sustainable, and eco-friendly system designed to harness solar energy for crucial environmental remediation applications. The developed YZBO−3 catalyst showed excellent degradation of LVF (98.5%) under sunlight at room temperature and atmospheric conditions, making it a very viable and cheap process for the removal of LVF from water. Although the developed photocatalyst showed excellent reusability and stability, offering a sustainable path toward a green economy, there are a few significant limitations that may hinder its widespread industrial application. The primary challenges include low energy conversion efficiency, limited light absorption, and the diurnal and weather-dependent nature of sunlight, which make it difficult to maintain a constant, efficient, and reproducible photocatalytic performance. The separation and recovery of the catalyst particles from the treated effluent present a significant engineering challenge.

Future research should include doping of spinel oxides with other rare-earth metals to maximize the TOC reduction, and include other types of antibiotics, as photodegradation performance is also dependent on the chemical structure of antibiotics. Their performance in the presence of other additives in effluent containing drugs and multiple drugs needs to be studied. The removal of the used photocatalyst from the treated effluent is also cumbersome. To ease their removal, sometimes catalysts are immobilized on various supports. It is necessary to conduct further research to determine whether that kind of immobilization affects the photocatalytic performance of the photocatalyst developed in this work.

The proposed photocatalytic mechanism is primarily based on indirect experimental evidence, such as scavenger studies and optical analysis. More advanced techniques, including electron spin resonance (ESR) and electrochemical measurements, would provide deeper insight into the charge transfer pathways and reactive species generation. In addition, the experiments were carried out using model aqueous solutions of levofloxacin. The presence of competing ions, natural organic matter, and multiple contaminants in real wastewater may influence the photocatalytic efficiency and should be investigated in future studies. Future research should focus on improving catalyst design, exploring other rare-earth dopants, evaluating performance in complex wastewater systems, and developing scalable reactor systems for real environmental applications.

5. Conclusions

Pure and Y-doped Zinc bismuth oxide ($ZnBi_2O_4$) were synthesized by the hydrothermal method with 0, 1, 3, and 5 mol% of yttrium. Yttrium doping induced structural modification and lattice distortion, as evidenced by changes in the diffraction patterns and Raman spectra. The surface morphology and elemental composition were investigated using scanning electron microscopy and energy-dispersive X-ray spectroscopy.

UV-Visible spectroscopy in the range of 200–800 nm was used for optical analysis. The optical behavior of synthesized nanostructures was confirmed by photoluminescence (PL) spectrum, visible emissions with different intensity and peak position with an increase or decrease in the yttrium content. The photocatalytic performance of the synthesized photocatalyst was evaluated by photocatalytic removal of levofloxacin under sunlight. A significantly increased photocatalytic performance was observed for the Y-doped $ZnBi_2O_4$ compared to the pristine $ZnBi_2O_4$, demonstrating that Y-doping substantially increased the photocatalytic performance of $ZnBi_2O_4$. The increased optical and photocatalytic characteristics imply that the YZBO−3 photocatalyst is highly promising in terms of further applications in the fields of photocatalysis. The analysis after the 5th cycle, such as XRD and SEM, further confirmed the excellent structural stability and durability of the photocatalyst after repeated cycles.

CRediT authorship contribution statement

Mohammad Mahbubul Hassan: Writing – review & editing, Validation. **Wesam Abd El-Fattah:** Resources. **Muhammad Asam Raza:** Writing – review & editing. **Adnan Ashraf:** Supervision, Resources, Conceptualization. **Muhammad Naeem:** Writing – review & editing, Methodology. **Maryam Rao:** Writing – original draft.

Declaration of Competing Interest

The authors declare that they have no known competing financial interests or personal relationships that could have appeared to influence the work reported in this paper.

Acknowledgement

We thank The University of Lahore (Pakistan) for providing research facilities to conduct this research. Wesam Abd El-Fattah was financially supported by the Deanship of Scientific Research grant of the Mohammad Ibn Saud Islamic University (Grant # IM-SIU DDRSP2503).

Data availability

Data will be made available on request.

References

[1] M. Naeem, M. Imran, S. Latif, A. Ashraf, N. Hussain, G. Boczkaj, W. Smułek, T. Jesionowski, M. Bilal, Multifunctional catalyst-assisted sustainable reformation of lignocellulosic biomass into environmentally friendly biofuel and value-added chemicals, Chemosphere 330 (2023) 138633, https://doi.org/10.1016/j.chemosphere.2023.138633.

[2] M. Naeem, F. Haider, A. Ashraf, S. Ahmed, K.M. Batoo, W.A. Siddiqui, M. Imran, M. A. Raza, M. Pervaiz, S. Hussain, Facile development of copper ferrite nanospheres for UV light-driven photocatalytic degradation of cloxacillin sodium, Mater. Adv. 5 (2024) 369–378, https://doi.org/10.1039/D3MA00677H.

[3] D.H.K. Reddy, Y.-S. Yun, Spinel ferrite magnetic adsorbents: alternative future materials for water purification? Coord. Chem. Rev. 315 (2016) 90–111, https://doi.org/10.1016/j.ccr.2016.01.012.

[4] M.M. Hassan, C.M. Carr, Biomass-derived porous carbonaceous materials and their composites as adsorbents for cationic and anionic dyes: a review, Chemosphere 265 (2021) 129087, https://doi.org/10.1016/j.chemosphere.2020.129087.

[5] A. Modabberasl, T. Pirhoushyaran, S.H. Esmaeili-Faraj, Synthesis of $CoFe_2O_4$ magnetic nanoparticles for application in photocatalytic removal of azithromycin from wastewater, Sci. Rep. 12 (2022) 19171, https://doi.org/10.1038/s41598-022-21231-2.

[6] R. Xu, K. Qian, X. Xie, J. Chen, W. Tang, F. Tao, Y. Wang, In situ degradation of fluoroquinolone antibiotics in groundwater by $CoFe_2O_4$ nanoparticle-activated peroxymonosulfate: performance, activation mechanism, degradation pathway, Appl. Geochem. 152 (2023) 105605, https://doi.org/10.1016/j.apgeochem.2023.105605.

[7] J.O. Eniola, R. Kumar, M.A. Barakat, Adsorptive removal of antibiotics from water over natural and modified adsorbents, Environ. Sci. Pollut. Res. 26 (2019) 34775–34788, https://doi.org/10.1007/s11356-019-06641-6.

[8] N. Pathania, S. Kumari, K. Thakur, S. Kulshrestha, R. Khargotra, Advancements in microalgae-mediated technologies for antibiotic removal from wastewater: a review, Biodegradation 37 (2026) 54, https://doi.org/10.1007/s10532-026-10273-2.

[9] S. Safaei, S.A. Mirbagheri, M. Ehteshami, E. Teymouri, M. Salari, Removal of antibiotics from wastewater by comparison of coagulation, membrane and adsorption methods, Jordan. J. Civil. Eng. 17 (2023), https://doi.org/10.14525/JJCE.v17i3.10.

[10] F. Yin, S. Lin, X. Zhou, H. Dong, Y. Zhan, Fate of antibiotics during membrane separation followed by physical-chemical treatment processes, Sci. Total. Environ. 759 (2021) 143520, https://doi.org/10.1016/j.scitotenv.2020.143520.

[11] Z. Yang, Y. Huang, X. Li, Z. Jiang, Y. Chen, S. Yang, H.F. Garces, Y. Sun, K. Yan, Highly dispersed $CoFe_2O_4$ spinel on biomass-derived 3D porous carbon framework for much enhanced Fenton-like reactions, Separat. Purif. Technol. 298 (2022) 121535, https://doi.org/10.1016/j.seppur.2022.121535.

[12] X. Bai, W. Chen, B. Wang, T. Sun, B. Wu, Y. Wang, Photocatalytic degradation of some typical antibiotics: recent advances and future outlooks, Int. J. Mol. Sci. 23 (2022) 8130, https://doi.org/10.3390/ijms23158130.

[13] H. Wang, X. Li, X. Zhao, C. Li, X. Song, P. Zhang, P. Huo, A review on heterogeneous photocatalysis for environmental remediation: from semiconductors to modification strategies, Chin. J. Catal. 43 (2022) 178–214, https://doi.org/10.1016/S1872-2067(21)63910-4.

[14] J. You, Y. Guo, R. Guo, X. Liu, A review of visible light-active photocatalysts for water disinfection: features and prospects, Chem. Eng. J. 373 (2019) 624–641, https://doi.org/10.1016/j.cej.2019.05.071.

[15] K. Qin, D. Zang, Y. Wei, Polyoxometalates based compounds for green synthesis of aldehydes and ketones, Chin. Chem. Lett. 34 (2023) 107999, https://doi.org/10.1016/j.cclet.2022.107999.

[16] S. Das, S. Kumar, S. Sarkar, D. Pradhan, C.S. Tiwary, S. Chowdhury, High entropy spinel oxide nanoparticles for visible light-assisted photocatalytic degradation of binary mixture of antibiotic pollutants in different water matrixes, J. Mater. Chem. A 12 (2024) 16815–16830, https://doi.org/10.1039/D4TA02294G.

[17] H.H. Cho, J. Yang, J.K. Kim, M.H. Kim, H.K. Yu, High-entropy spinel oxide: synthesis and photo-responsivity of $Mn_{0.68}Cr_{0.8}Rh_{0.64}Co_{0.87}O_4$, J. Alloy. Comp. 1010 (2025) 176969, https://doi.org/10.1016/j.jallcom.2024.176969.

[18] A.M. Djaballah, R. Bagtache, M. Trari, Physical and electrochemical properties of the spinel $ZnBi_2O_4$ prepared by citrate route: application towards photo degradation of methyl violet, J. Mater. Sci. Mater. Electron. 33 (2022) 18410–18419, https://doi.org/10.1007/s10854-022-08695-8.

[19] A.R. Tony, A.V.J. Verjhula, Yttrium doped magnesium ferrite nanoparticles: a potential solar light driven photocatalyst for deterioration of hazardous dyes, J. Mater. Sci. Mater. Electron. 35 (2024) 481, https://doi.org/10.1007/s10854-024-12160-z.

[20] A. Quddus, S.Z.H. Hashmi, G. Mustafa, M. Khalid, M.G.B. Ashiq, G. Nazir, T. M. Alshahrani, M.S. Alqahtani, K. Naz, Sol-Gel synthesis of Ni-doped Zn-based spinel nanoferrites with structural and dielectric characterizations along with magnetic analysis, Colloid Surf. Sci. A Physicochem. Eng. Asp. 676 (2023) 132074, https://doi.org/10.1016/j.colsurfa.2023.132074.

[21] U. Alam, A. Khan, D. Ali, D. Bahnemann, M. Muneer, Comparative photocatalytic activity of sol–gel derived rare earth metal (La, Nd, Sm and Dy)-doped ZnO photocatalysts for degradation of dyes, RSC Adv. 8 (2018) 17582–17594, https://doi.org/10.1039/C8RA01638K.

[22] M. Rao, A. Ashraf, M. Naeem, J.Z. Arshad, M. Khan, S. Ahmed, M. Pervaiz, M. Farhan, M.A. Raza, Visible light-driven degradation of levofloxacin by europium-doped zinc bismuth spinel oxide, ChemistrySelect 11 (2026) e07114, https://doi.org/10.1002/slct.202507114.

[23] M. Rao, A. Ashraf, M. Naeem, N. Majeed, W.Abd El-Fattah, M.A. Raza, Visible light activated Sm-Doped $ZnBi_2O_4$ spinel oxide for efficient degradation of moxifloxacin from wastewater, Surf. Interf. 87 (2026) 108874, https://doi.org/10.1016/j.surfin.2026.108874.

[24] A.U.R. Khan, M. Ramzan, S.J. Alanazi, A.M. Al-Mohaimeed, S. Ali, M. Imran, M. A. Majid, M.H. Sarfraz, Structural, optical, electrical and photocatalytic investigation of n-type Zn^{2+}-doped α-Bi_2O_3 nanoparticles for optoelectronics applications, ACS Omega 9 (2024) 22650–22659, https://doi.org/10.1021/acsomega.3c10521.

[25] J. Ye, X. Wang, D. Yu, F. Ai, S. Yu, J. Shen, S. Lu, Q. Xiao, S. Li, Q. Xie, Enhanced Photocatalytic, mechanical, and optical performance of rare-earth–doped Mg_2Si: First-principles calculations and machine learning, Appl. Organomet. Chem. 39 (2025) e70396, https://doi.org/10.1002/aoc.70396.

[26] B. Xu, L. Wang, M. Yang, Y. Xiang, L. Liu, Effect of co-doping of Al^{3+}, In^{3+}, and Y^{3+} on the electrical properties of zinc oxide varistors under pre-synthesizing $BiSbO_4$, Materials 17 (2024) 1401, https://doi.org/10.3390/ma17061401.

[27] R. Sharma, Komal, V. Kumar, S. Bansal, S. Singhal, Boosting the catalytic performance of pristine $CoFe_2O_4$ with yttrium (Y^{3+}) inclusion in the spinel structure, Mater. Res. Bull. 90 (2017) 94–103, https://doi.org/10.1016/j.materresbull.2017.01.049.

[28] R. Verma, S.N. Kane, S. Raghuvanshi, M. Satalkar, S.S. Modak, F. Mazaleyrat, Synthesis, structural and magnetic properties of $Mg_{0.6}Zn_{0.4}Cr_xFe_{2-x}O_4$ ($0.0 \leq x \leq 2.0$) nano ferrite, AIP Conf. Proc 1953 (2018) 030135, https://doi.org/10.1063/1.5032470.

[29] M. Córdoba, M. Berruet, K. Taretto, Reassessing the interpretation of current/voltage and steady–state photocarrier grating measurements in $CH_3NH_3PbI_3$ perovskite films across device-operation temperatures, J. Phys. Chem. Solid. 207 (2025) 112961, https://doi.org/10.1016/j.jpcs.2025.112961.

[30] C. Yang, Z. Liu, Z. Su, Y. Wang, M. Liang, H. Fan, T.J. Bandosz, Combined effect of oxygen vacancies and mesopore sizes in ZnO/SiO_2 adsorbents on boosting the H_2S removal efficiency in moist conditions, Adv. Func. Mater. 34 (2024) 2409214, https://doi.org/10.1002/adfm.202409214.

[31] A. Horváth, A. Beck, M. Németh, G. Sáfrán, M. Roškarič, G. Žerjav, A. Pintar, Influence of 0.25% indium addition to Ni/CeO_2 catalysts for dry reforming of methane, Catalysts 14 (2024) 383, https://doi.org/10.3390/catal14060383.
[32] A. Chetoui, I. Belkhettab, A. Elfiad, Y. Messai, A. Ziouche, M. Tablaoui, An in-depth photoluminescence investigation of charge carrier transport in $ZrO_2|V_2O_5$ type I junction: Probing the production of hydroxyl radicals, Appl. Surf. Sci. 646 (2026) 158947, https://doi.org/10.1016/j.apsusc.2023.158947.
[33] W. Kong, H. Jiang, X. Chen, B. Chen, H. Wang, Z. Shi, L. Chen, J. Wen, P. He, J. Wu, J. Lin, Visible-light triggered Sm^{3+}/Sm^{2+} valence cycling in BiOBr photocatalysts for enhanced electron transfer and mercury removal, J. Taiwan. Inst. Chem. Eng. 181 (2026) 106515, https://doi.org/10.1016/j.jtice.2025.106515.
[34] PR Griffiths, B.E. Fries, A.T. Weakley, On the widths of bands in the infrared spectra of oxyanions, Appl. Spectros. 72 (2018) 863–869, https://doi.org/10.1177/0003702818764446.
[35] N.T.M. Tho, D.N.N. Khanh, N.Q. Thang, Y.-I. Lee, N.T.K. Phuong, Novel reduced graphene oxide/$ZnBi_2O_4$ hybrid photocatalyst for visible light degradation of 2,4-dichlorophenoxyacetic acid, Environ. Sci. Pollut. Res. 27 (2020) 11127–11137, https://doi.org/10.1007/s11356-020-07752-1.
[36] L. Mllaoiy, B. Bakiz, A. Bouddouch, S. Villain, A. Taoufyq, F. Guinneton, J.-R. Gavarri, A. Benlhachem, Construction of p-$ZnBi_2O_4$/n-BiOBr heterojunctions for efficient visible-light photocatalytic degradation of dyes, Mater. Adv. 7 (2026) 1790–1804, https://doi.org/10.1039/D5MA00892A.
[37] G. Yuan, M. Li, M. Yu, C. Tian, G. Wang, H. Fu, In situ synthesis, enhanced luminescence and application in dye sensitized solar cells of Y_2O_3/Y_2O_2S: Eu^{3+} nanocomposites by reduction of Y_2O_3:Eu^{3+}, Sci. Rep. 6 (2016) 37133 https://doi.org/10.1038/srep37133.
[38] N. Chen, L. Gou, M. Hu, C. Wang, L. Tan, D. Zhao, H. Feng, Hierarchical 0D/3D Z-scheme heterojunction of ZnO quantum dots/flower-like Bi_2MoO_6 microspheres for efficient photocatalytic degradation of tetracycline, New. J. Chem. 49 (2025) 13024–13040, https://doi.org/10.1039/D5NJ01633A.
[39] Y. Wang, Y. Kang, X. Liu, Construction of visible-light-driven $ZnBi_2O_4/Ag_2WO_4$ p–n heterojunction for restraining carrier recombination and improving visible-light photocatalytic performance, J. Mater. Sci. Mater. Electron. 33 (2022) 19827–19838, https://doi.org/10.1007/s10854-022-08796-4.
[40] P.F. Lang, Revisiting electronegativity and electronegativity scales, J. Chem. Educ. 102 (2024) 424–429, https://doi.org/10.1021/acs.jchemed.4c01353.
[41] Z. Zafar, S. Yi, J. Li, C. Li, Y. Zhu, A. Zada, W. Yao, Z. Liu, X. Yue, Recent development in defects engineered photocatalysts: an overview of the experimental and theoretical strategies, Energ. Environ. Mater. 5 (2022) 68–114, https://doi.org/10.1002/eem2.12171.
[42] R.U. Syed, K.M. Younes, H. Banu, W.M.A. Khojali, N.A.E. Masood, F.M. Alsaiari, S. Saddeek, I. Shakir, M. Aadil, Hydrothermally synthesized W-doped CuS nanostructures with tunable structural and optoelectronic properties for redox-driven photocatalysis and antimicrobial activity, J. Alloy. Compd. 1060 (2026) 187338, https://doi.org/10.1016/j.jallcom.2026.187338.
[43] M. Elhadi, M.A. Rafea, N. Mustapha, M.E.A. Zaki, S. Saddeek, M. Sattar, M.R. El-Aassar, M. Aadil, Enhanced photocatalytic performance of Sr-doped $NiFe_2O_4$ nanostructures synthesized via a surfactant-assisted wet-chemical route, Ceram. Int. 51 (2025) 62711–62722, https://doi.org/10.1016/j.ceramint.2025.10.434.
[44] A. Tolosana-Moranchel, C. Pecharromán, M. Faraldos, A.M. Bahamonde, Strong effect of light scattering by distribution of TiO_2 particle aggregates on photocatalytic efficiency in aqueous suspensions, Chem. Eng. J. 403 (2021) 126186, https://doi.org/10.1016/j.cej.2020.126186.
[45] T.V.H. Luu, V.C. Nguyen, T.D.T. Tran, V.D. Doan, T.L. Nguyen, N.X. Dung, H. P. Dang, A novel 3D Fe_2O_3@$ZnBi_2O_4$ n–p heterojunction with high photocatalytic activity under visible light, Nanoscale Adv. 7 (2025) 2942, https://doi.org/10.1039/D4NA01039F.
[46] M.I. Rameel, M. Wali, J.Y. Al-Humaidi, F. Liaqat, M.A. Khan, Enhanced photocatalytic degradation of levofloxacin over heterostructured C_3N_4/Nb_2O_5 system under visible light, Heliyon 9 (2023) e20479, https://doi.org/10.1016/j.heliyon.2023.e20479.
[47] F. Bibi, M. Zubair, A. Kalsoom, I. Hossain, K. Yasmeen, E. Aldosari, Q. Raza, M. Mahmood, S. Iqbal, Development of a high-performance La/Cu Co-doped $BiFeO_3$/g-C_3N_4 nanocomposite for efficient degradation of moxifloxacin and crystal violet dye for environmental applications, J. SolGel Sci. Technol. 116 (2025) 3030–3053, https://doi.org/10.1007/s10971-025-06990-4.